HYDROTHERMAL VENTS AND THEIR IMPACT ON PALEOENVIRONMENTAL PROXIES

By

ALISON VERESH

Bachelor of Science in Environmental Science

Central Michigan University

Mount Pleasant, MI

2020

Submitted to the Faculty of the
Graduate College of the
Oklahoma State University
in partial fulfillment of
the requirements for
the Degree of
MASTER OF SCIENCE
December, 2022

HYDROTHERMAL VENTS AND THEIR IMPACT ON

PALEOENVIRONMENTAL PROXIES

Thesis Approved:

Dr. Natascha Riedinger

Thesis Adviser

Dr. Ashley Burkett

Dr. Tracy Quan

ACKNOWLEDGEMENTS

Thank you so much to everyone who helped me out throughout this graduate school journey. Thank you to my advisor, Dr. Natascha Riedinger, and my committee, Dr. Tracy Quan and Dr. Ashley Burkett. Thank you to the Captain, and crew of the Polarstern and the scientists of PS119, especially Dr. Gerhard Bohrmann, the geochemistry group of Dr. Marta Torres, Anna Lichtschlag, and Male Köster. Thank you to Chris Jones and Lauren Haygood for running my samples at the University of California -Riverside. Thank you to my family and friends, for supporting me through the past 2 years.

Acknowledgements reflect the views of the author and are not endorsed by committee members or Oklahoma State University.

Name: ALISON VERESH

Date of Degree: DECEMBER, 2022

Title of Study: HYDROTHERMAL VENTS AND THEIR IMPACT ON PALEOENVIRONMENTAL PROXIES

Major Field: GEOLOGY

Abstract: Trace metals such as cobalt, copper, molybdenum, and uranium have been used as redox and productivity proxies to interpret paleoenvironments. However, the presence of a hydrothermal vent could potentially alter the interpretations if metal-rich fluids from these vents serve as another source for these specific trace metals into the sediment. To date, there are no published studies on the impact of hydrothermal vent deposits on paleoproxies. In this thesis the impact of hydrothermal vents on trace metal deposition in the surrounding sediments was investigated. Two cores were compared for their elemental composition applying a multi-acid total digestion and inductively coupled plasma mass spectrometry analysis. The comparison was carried out on samples collected during the RV Polarstern Expedition PS119 in the Scotia Sea, on a core collected on the east side of an ocean ridge containing a hydrothermal vent field and another core from the west side of the ridge. The direction of the Antarctic Circumpolar Current is from west to east in the Scotia Sea. Thus, only the site on the east side of the hydrothermal vent could potentially receive hydrothermal vent plume deposits. Concentrations of the proxies, specifically molybdenum, copper, and cobalt are higher in the core on the east side of the hydrothermal vent field than the core on the west side. While there are a few potential sources of the enrichment, the most likely cause is hydrothermal vent input. Other sources of metal enriched layers include volcanic ash deposits or diagenetic alteration. The findings of this study highlight that hydrothermal vent deposits need to be regarded in the interpretation of paleo-redox and productivity proxies in the ancient rocks deposited near active ocean ridges.

TABLE OF CONTENTS

LIST OF TABLES

Table Page

LIST OF FIGURES

Figure Page

CHAPTER I

INTRODUCTION

Past studies have investigated the impact of hydrothermal vent fluids on the biogeochemical cycling of trace metals in the ocean in the water column (German et al. 2016, Sander and Koschinsky 2011, Yucel et al. 2011). Hydrothermal vent fluids are enriched and depleted in specific trace metals relative to seawater and these fluids mix with seawater, serving as source of trace elements (German et al. 2016, SCOR Working Group 2006, German and Seyfried 2014, Sander and Koschinsky 2011). These vent fluids were recognized as one of four important sources of trace element flux to and from the ocean by the GEOTRACES Program (German et al. 2016, SCOR Working Group 2006). The presence of hydrothermal vents has the potential to affect the paleoenvironmental interpretations in sediments receiving vent fluid input. In this project the effects of hydrothermal vent fluids on redox and productivity proxies in surrounding sediments were investigated. Sediment cores from the Scotia Sea were analyzed for two productivity proxies, copper and cobalt, and two redox proxies, molybdenum and uranium.

CHAPTER II

REVIEW OF LITERATURE

Hydrothermal Vents

Hydrothermal vents are created when water percolates into fractured ocean crust, where it reacts with rock and is chemically modified and heated up by the interior of the Earth (Yücel et al. 2011, Rodgers et al. 2012, Hawkes et al. 2013, German and Seyfried 2014). As the hot seawater becomes more buoyant, it rises back up to the ocean floor and is expelled back into the ocean water column (Rodger et al. 2012, Hawkes et al. 2013, German and Seyfried 2014). A type of hydrothermal vents called 'black smokers', emit clouds of black plumes formed from the chemicals precipitating from the venting seawater upon mixing with the bottom waters and forming metal sulfide and oxide mineral rich deposition (Yücel et al. 2011, German and Seyfried 2014, German et al. 2016). The composition of hydrothermal vent fluids is determined by phase separation, water-rock interactions, and magmatic degassing (Pereira et al. 2022). Water-rock interactions and phase separation occurs throughout the hydrothermal system, starting with the recharge zone where seawater enters the oceanic crust and continues until it is discharged out of the sheeted dike complex back into the ocean (German and Seyfried 2014, Pereira et al. 2022). The pathway at which water-rock interactions and phase separation occurs is called the root zone (German and Seyfried 2014, German et al. 2016). Chemical species are gained and lost at both recharge and discharge limbs of the root system from water-rock interactions (German and Seyfried 2014, Pereira et al. 2022). For example, dissolved sulfate in seawater is lost in the

recharge section of the root system through the creation of anhydrite at 130 ºC as seawater is heated by the mantle beneath (German and Seyfried 2014, Pereia et al. 2022). The two main components of seawater are H2O and NaCl and using the phase diagram for these components and pressure and temperature, one can determine if phase separation will result in vent fluid more enriched or depleted, in chloride relative to seawater (Bischoff and Rosenbauer 1985).

When high temperature hydrothermal vent fluids exit the vent, there are three fluid sources that contribute to the resulting plume (Figure 1). The first source of fluids is the vent fluid that has emitted out of the black smoker. Hydrothermal fluid contains many metals from the reactions that occur inside the hydrothermal vent such as phase separations and water rock interactions from basaltic rocks (Sander and Koshinsky 2011, German and Seyfried 2014). The hot temperature of the hydrothermal vent fluid makes the plume buoyant (Helfrich and Speer 1995, German et al. 2015).

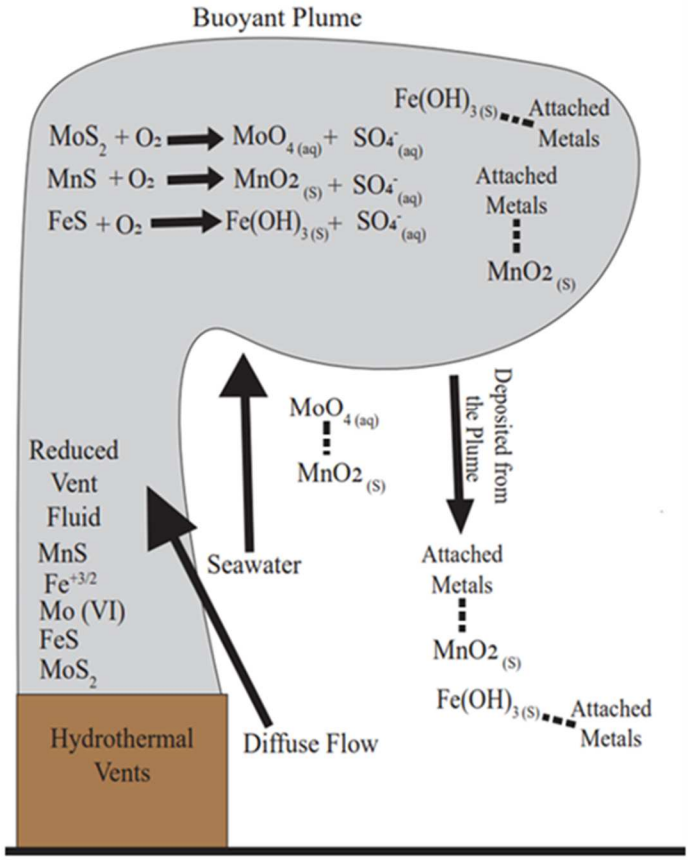

Figure 1: Schematic diagram of chemical reactions occurring inside a hydrothermal vent plume. Black dashed lines indicate adsorption. Arrows are chemical reactions or transportation in and out of the plume.

Deep ocean seawater and diffuse flow of hydrothermal fluids are entrained into the plume as it rises (Sander and Koshinksky 2011, German et al. 2015, Pereira et al. 2022). An average hydrothermal vent is diluted at a 10,000:1 ratio by the seawater and diffuse flow (German et al. 2015). When hydrothermal vent fluid encounters seawater, iron, manganese, and iron and manganese sulfides in the fluid oxidize and form oxyhydroxide particles (Mandernack and Tebo 1993, Hawkes et al. 2013). These oxyhydroxide particles attract dissolved metals from the seawater and oxidized metals from the vent fluid and adsorb to them (Hrischeva and Scott 2007, Hawkes et al. 2013). The metals attached to the oxyhydroxides are carried in the plume until they

fall out of the plume and are deposited into the sediment (Figure 1) (Sander and Koschinsky 2011, German et al. 2015).

Redox Proxies

Redox proxies are used to provide information about levels of oxidation in the bottom waters during the time of deposition by observing the concentrations of trace metals used in redox reactions (e.g., Lyons et al. 2009, Algeo and Lui 2020, Bennet and Canfield 2020). The environment is then classified based on oxygen availability using the terms oxic, suboxic, anoxic, and euxinic (e.g, Algeo and Maynard 2004). Generally, oxic environments are >2.0 ml O_2/L, dysoxic or suboxic environments are 0.2–2.0 ml O_2/L, anoxic–non-sulfidic environments are <0.2 ml O_2/L with 0 ml H_2S/ L and anoxic–sulfidic or euxinic environments are 0 ml O_2/L with >0 ml H_2S/L (Algeo and Tribovillard 2009). Abiotic and biotic processes both remove these redox-sensitive metals from the water column and transport them to the sediment to be preserved in the sediment record (Tribovillard et al. 2006, and references therein). Many trace metals are deposited to the sea floor by authigenic sulfides, organic complexation, or attachment to Mn and Fe (oxyhydr)oxides (e.g., Alego and Maynard 2004, McManus et al. 2006, Steiner et al. 2017).

In suboxic sediment, marine organic matter is oxidized by iron and manganese oxides (Froelich et al. 1979) (Equation 1 and 2):

Equation 1: $(CH_2O)_{106}\ (NH_3)_{16}\ (H_3PO_4) + 236\ MnO_2 + 472\ H^+ \rightarrow 236\ Mn^{2+} + 16\ HNO_3 + H_3PO_4 + 8\ N_2 + 366\ H_2O$

Equation 2: $(CH_2O)_{106}\ (NH_3)_{16}\ (H_3PO_4) + 212\ Fe_2O_3$ (or 424 FeOOH) + 848 $H^+ \rightarrow 424\ Fe^{2+} + 106\ CO_2 + H_3PO_4 + 530\ H_2O$ (or 742 H_2O)

The reduction of these oxides release manganese and iron into the pore waters as well as metals that have adsorbed to the oxides (Froelich et al. 1979, Halbach et al. 1988). The manganese and iron can then re-oxidize. (Froelich et al. 1979, Halbach et al. 1988).

Molybdenum

Molybdenum (Mo) is often used as a proxy for detecting sulfide in the water and is commonly found in the form molybdate (MoO_2^{4-}) (Morford and Emerson 1999, Lyons et al. 2009). Molybdenum is present in seawater at a concentration of about 105 nmol (e.g, Morford and Emerson 1999, Algeo and Maynard 2004, McManus et al. 2006). In oxic sediments, Mo is scavenged in association with metal oxides such as Mn hydroxides (Morford and Emerson 1999). In anoxic and sulfidic conditions, molybdate is converted to thiomolybdates ($MoO_XS_X^{4-}$) in the presence of dissolved H_2S (Helz et al. 1996, Morford and Emerson 1999, Lyons et al. 2009). Thus, molybdenum enrichment in the sediments occurs most commonly in sulfidic anoxic conditions (Algeo and Maynard 2004; Scott and Lyons 2012).

Uranium

Uranium is present in oxic conditions as U(VI) in unreactive uranyl carbonate complexes ($UO_2(CO_3)_3^{4-}$) and is present in seawater at concentrations of about 13 nM (McMannus et al. 2006). Under reducing water conditions, soluble uranium (VI) is reduced to insoluble uranium (IV) and sinks to the bottom of the water column (McMannus et al. 2006, Algeo and Tribovillard 2009, Abshire et al. 2020). Uranium can also be transported to the sediment via organic matter; however, the amount has been described as small but variable (McMannus et al. 2006). Uranium is not affected by Mn and/or Fe (oxyhydr)oxides (Algeo and Maynard 2004).

Productivity Proxies

Productivity is one of the most important factors influencing the ability of the ocean to remove carbon dioxide from the atmosphere (Berger et al. 1989). Bio-essential elements can be used as paleoproductivity proxies to track changes in productivity and redox conditions (e.g., Swanner et al. 2014). Productivity proxies are used because organic matter buried in the sediment represents only about 10% of productivity that occurred in the marine photic zone (Berger et al. 1989).

Copper

Copper is biologically essential for many organisms but can also be toxic if exceeding certain concentrations levels (Little et al. 2017). It is used as a productivity proxy in the sediment record because the main form of transport of copper to the sediment is through the settling of organic matter, which makes it a good proxy to measure organic matter flux (Steiner et al. 2017). In oxic water, copper is mainly present as organometallic ligands and $CuCl^+$ ions (Calvert and Pedersen 1993). Copper can be reduced by sulfides with or without Fe to form CuS and CuS_2 (Morse and Luther 1999). Copper binds to Mn and Fe-(oxyhydr)oxides as well as to organic ligands (Fernex et al. 1992, Bruland 2003). In the water column, concentrations of copper are depleted and increase in concentration with depth and high concentrations at the sediment-water interface (Calvert and Pedersen 1993). Copper is an essential micronutrient but is also scavenged in deep water (Calvert and Pederson 1993). Enriched concentrations of copper have been found in the vent fluids of some hydrothermal vents (German and Seyfried 2014).

Cobalt

Cobalt is used in forming the central cobalt-corrin complex of cobalamin (vitamin B12) and is directly bound in enzymes such as nitrile hydratase (Swanner et al. 2014). Concentrations of cobalt in seawater vary from 3 to 120 pM and display nutrient-like distributions (Swanner et al. 2014). Approximately 90% of cobalt in the ocean exists in strong cobalt-binding organic ligands

(Bruland 2003). Cobalt exists in either the divalent or trivalent form and is insoluble in the trivalent state (Saito et al. 2004). Data from Hrishceva and Scott 2007 shows a correlation between Co and Fe in hydrothermal sediments from the Juan de Fuca Ridge, which supports the pathway for Co to be absorbed to Fe (III) (oxyhydr)oxides (Swanner et al. 2014).

A summary of important information about the four applied proxies is provided below (Table 1).

Table 1: Summary of the four paleo-proxies applied in this study.

Characteristic	**Molybdenum (Mo)**	**Uranium (U)**	**Copper (Cu)**	**Cobalt (Co)**
Productivity or Redox Proxy	Redox	Redox	Productivity	Productivity
Biologically Essential	Yes, toxic at high levels	No	Yes, toxic at high levels	Yes
Main Species in Oxic Seawater	Molybdate	uranyl carbonate complexes U(VI)	Cu (II)	Co (III)
Average Concentration in Seawater (nmol/kg)	105	13.4	2.36	0.02
Main Species in Reducing Conditions	Thiomolybdates	U(IV)	Cu (I)	Co (II)
Main Mechanism for Incorporation into Sediment	Scavenged by metal oxides in oxic conditions, in reducing systems, Mo is converted to thiomolybdates and scavenged via organic S-rich material	Removal from the water column by reduction of U(VI) and formation of organometallic ligands	Attached to settling organic matter, scavenged through sulfurization	Scavenged by Mn (II)-oxidizing bacteria, Attached to Mn-oxyhydroxides
Absorbs to iron and manganese oxyhydroxides	Yes	No	Yes	Yes

CHAPTER III

METHODOLOGY

Study Site

The East Scotia Ridge (ESR) is a spreading ridge, moving at a rate of 65-70 mm/year (German et al. 2000) (Figure 2). The hydrothermal vents in this study are back-arc basin (BAB) hydrothermal vents opposed to the common mid-ocean ridge hydrothermal systems (James et al. 2014, Pereira et al. 2022). The East Scotia Ridge hydrothermal vents are the only BAB vents not located in the Pacific Ocean (Pereira et al. 2022). The ridge separates the Sandwich Plate to the west from the Antarctic Plate to the east. It is approximately 500 km long (Rodgers et al. 2012). The East Scotia Ridge is and made up of 9 non-transform discontinuities (German et al. 2000, Rodgers et al. 2014). The E2 and E9 segments contain the most hydrothermal activity (Hawkes et al. 2013). The E2 segment has axial volcanic ridges, which are a type of composite volcano made of built-up accumulation of volcanic hummocks parallel to the ridge with shallow magma chambers (only 2-3 km) (Yeo 2012, James et al. 2014, Bohrmann 2019). The E2 vent field is located between 56º 5.2'S and 56º 5.4'S and between 30º19 W and 30º 19.3'W (James et al. 2014). It has large vertical displacements running north to south (Hawkes et al. 2013). The hydrothermal vents are located approximately 2,600 m deep and consist of black smokers that release hot (>350°C), sulfide-rich fluids (Bohrmann 2019). The hydrothermal fluid plumes in E2 rise approximately 400 m above the vent (Hawkes et al. 2013). Fluids of the E2 vents can have a temperature of up to 351ºC at active venting chimneys (James et al. 2014).

Diffuse flow of hydrothermal fluids in the vent field is cooler at 3.5ºC to 20ºC (the temperature of the surrounding seawater is approximately 0.005 ºC) (James et al. 2014). The E2 hydrothermal vent fluids were depleted in chloride relative to seawater (Pereira et al. 2022). The 2009 expedition on the RRS James Clark Ross of the E2 vent fields measured the vent fluids and reported high concentrations of Mn (2,050- 2,220 µmol/kg) (James et al. 2014). The dissolved oxygen concentrations near the vents at E2 were approximately 200 µmol/kg (Hawkes et al. 2013). High Fe concentrations were also reported at E2, especially in the lower part of the plume (Hawkes et al. 2013). It was suggested that around 30% of dissolved iron in hydrothermal plumes are present in a chemically labile form that can be transported by deep water currents (Hawkes et al. 2013).

The Antarctic Circumpolar Current (ACC) flows clockwise around Antarctica (Maldonado et al. 2015). The deeper current component of the ACC is called the Circumpolar Deep Water (CDW) (Maldonado et al. 2015). The ACC is important to global thermohaline circulation (Naveira-Garabato et al. 2002, Maldonado et al. 2015). Global thermohaline circulation occurs when cold and dense water from Antarctica to the lower latitudes to upwell in the warmer, less dense water (Mantyla and Reid 1983). The Scotia Sea is important to this process because it is a pathway for water from the Weddell Sea to the Atlantic Ocean (Naveira-Garabato et al. 2002). The Weddell Sea Deep Water current (WSDW) flows eastward and northward, mixing in with the CDW (Naveira-Garabato et al. 2002, Maldonado et al. 2015). The WSDW comes from the Weddell Gyre. The northward movement of the WSDW is restricted by interference from the CDW (Naveira-Garabato et al. 2002). The largest deep-water current in the Scotia Sea is the CDW, specifically the Lower CDW (LCDW) which is marked by a salinity maximum from North Atlantic Deep Water (NADW) mixing with the ACC (Mantyla and Reid 1983 and Naveira-Garabato et al. 2002). The CDW and WSDW are the main currents flowing through the

hydrothermal vent field, flowing from west to east at temperatures between 0.2ºC and 0.7ºC (Hawkes et al. 2013).

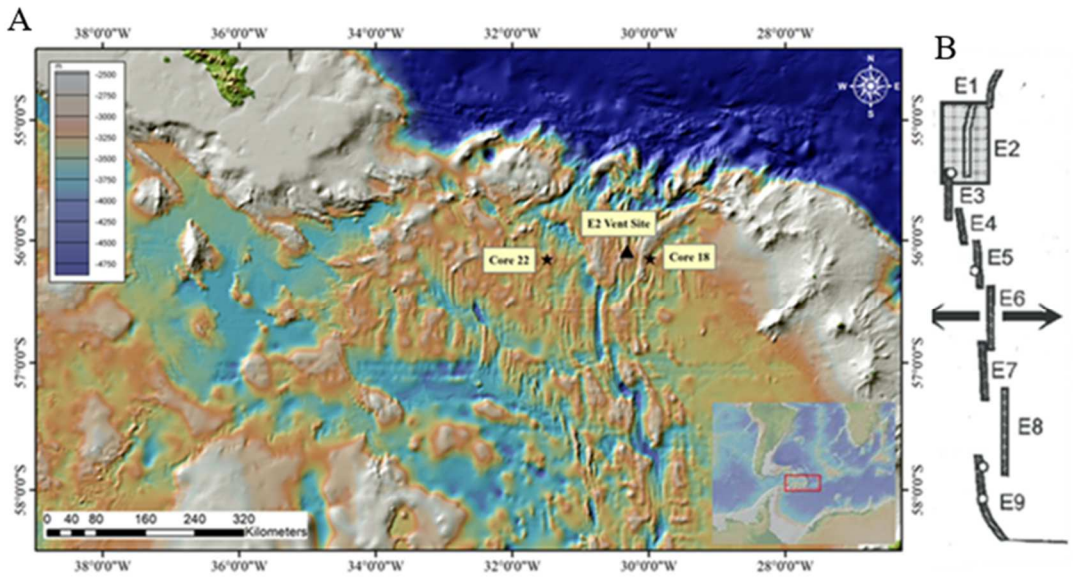

Figure 2: A. Map of the Scotia Sea with study locations marked. B. Diagram of the segments of the East Scotia Ridge. Segment E2 is boxed in grey (diagram by Leat et al. 2000).

Materials and Methods

Samples were collected during the RV Polarstern expedition PS119 in 2019 using a gravity corer (Bohrmann 2019). Site 18 is located at 56º08.95S and 29º58.54W, at a water depth of 3,266 m. Site 22 is located at 56º09.29S and 31º29.04W, at a water depth of 3,342 m (Bohrmann 2019). Site 22 is approximately 70 km southwest from the hydrothermal vents on E2. Site 18 is approximately 20 km southeast from the hydrothermal vent area (Figure 2).

After the cores were collected, they were sliced in half and the working half was stored in a cold room for sampling (Bohrmann 2019). Solid phase samples for geochemical analyses were taken using cut-off syringes and were stored in a freezer at -20°C. Core 18-2 contains 50 samples

ranging from depths of 8 cm to 484 cm at intervals between 10-20 cm. Core 22-1 contains 31 samples ranging from depths of 7 cm to 655 cm.

Sediment was first dried in an oven at 40°C and homogenized with an agate mortar and pestle. Dried sediment was then measured for sequential iron extraction, and approximately 0.100 g of sample is placed in PTFE vials. Trace metal grade (tmg) nitric (3 ml), perchloric (3 ml), and hydrofluoric acid (2 ml) was added to the sample and heated (see also Abshire et al. 2020). The sample and acids were boiled on a hot plate for 20 hours. The sample and acid mixture were evaporated down for 16 hours and then the samples were dissolved with a 5% nitric acid (tmg) solution and decanted into vials. Finally, the samples were analyzed at 10X and 100X dilution in a ThermoScientific iCAP QC Inductively Coupled Plasma Mass Spectrometer. The results from the 10X dilution were used in the results section of this study. Standard reference material NIST 2702, blanks, and a replicate sampled in each batched were also digested for quality control. A comparison of Mn concentrations of the three standard reference materials to the accepted values shows an error between 3% to 12%. The range of Mn concentrations of the replicate samples was 124 ppm and a standard deviation of 53 ppm. A comparison of Fe concentrations of the three standard reference materials to the accepted value shows an error between 1% to 15%. The range of Fe concentrations of the replicate samples was 8,895 ppm and a standard deviation of 3,770 ppm. A comparison of Mo concentrations of the three standard reference materials to the accepted value shows an error between 2% to 20%. The range of Mo concentrations of the replicate samples was 0.45 ppm and a standard deviation of 0.19 ppm(Table A5).

The second part of the methodology is sequential iron extraction. Frozen samples were first placed in centrifuge tubes and degassed with nitrogen before and after adding the acid solution to prevent the samples from oxidizing in the lab. Samples must be placed in centrifuge tubes to be spun down before decanting the extract to preserve sediment for the next extraction. An ascorbic acid solution was first added to the solution to extract the labile (readily available) forms of iron

such as ferrihydrite and lepidocrocite (Raiswell et al. 2010). The ascorbic acid solution is made from sodium citrate, sodium bicarbonate, ascorbic acid, and double deionized water (Raiswell et al. 2010). The sediment with the solution were then placed on a shaking table for 24 hours, and then centrifuged before decanting the extract into polyethylene containers. The second solution used in the procedure is sodium dithionite, which is made from sodium citrate, acetic acid, dithionite sodium hydrosulfite, and double deionized water (Poulton and Canfield 2005). The sodium dithionite extracts iron associated with crystalline oxides such as goethite (FeOOH) and hematite (Fe_2O_3) (Poulton and Canfield 2005). The sediment and solution were left on a shaking table for 2 hours before decanting. The third set in the sequence is a solution of ammonium oxalate, which is made of ammonium oxalate, oxalic acid, and double deionized water (Poulton and Canfield 2005). The ammonium oxalate solution extracts iron in magnetite (Fe_3O_4) (Poulton and Canfield 2005). An additional iron extraction was also carried out with separate centrifuge tubes of sediment using 0.5 M hydrochloric acid. The hydrochloric acid iron extraction method extracts amorphous Fe (III) oxides, FeS, non-S particulate Fe (II), and silicate Fe (Severmann et al. 2006). All four extractions were analyzed photometrically with a Ferrozine reagent with HEPES buffer and a photometer (Stookey 1970).

CHAPTER IV

RESULTS

All data reported in the results section can be found in the appendix (Table A1-A5).

Major Elements

The main peaks in the graph of manganese concentration in Core 18-2 are at 8 cm and 109 cm (Figure 3). Core 22-1 shows a large peak at 140 cm of 1,031 ppm of manganese (Figure 4). Overall, the general trend of manganese concentration remains constant throughout both Core 18-2 and Core 22-1, apart from the peaks (Figure 3 and Figure 4). Core 18-2 has a higher average manganese concentration compared to Core 22-1 by a difference of 1,232 ppm. The average can show magnitudes of differences in concentration between Core 22-1 and Core 18-2. It is important to take the average concentration without the peaks as background elemental concentration in Core 22-1 as seen later in the discussion.

The 109 cm and 8 cm concentration peaks are not seen in the Core 18-2 iron concentration graph. Instead, the concentration of iron in Core 18-2 exhibits no clear spikes throughout the core (Figure 3). There is a peak in the Core 22-iron concentration graph at 140 cm (Figure 4). Generally, both cores exhibit a general constant trend for iron concentration. Core 18-2 has a higher average concentration than Core 22-1 by a difference of approximately 0.7 weight percent (7,777 ppm).

The concentration of aluminum in Core 18-2 does not have a clear peak, behaving similarly to the iron and manganese concentrations in Core-18-2. Both aluminum concentration graphs for Core 18-2 and Core 22-1 behave similarly to the concentration graphs for iron and manganese, displaying a general constant trend (Figure 2 and Figure 3). Like the iron and manganese in Core 22-1, there is a peak at 140 cm in the concentration of aluminum for Core 22-1 (Figure 3). The average concentration of aluminum is higher in Core 18-2 by a difference of approximately 0.13 weight percent (3,319 ppm).

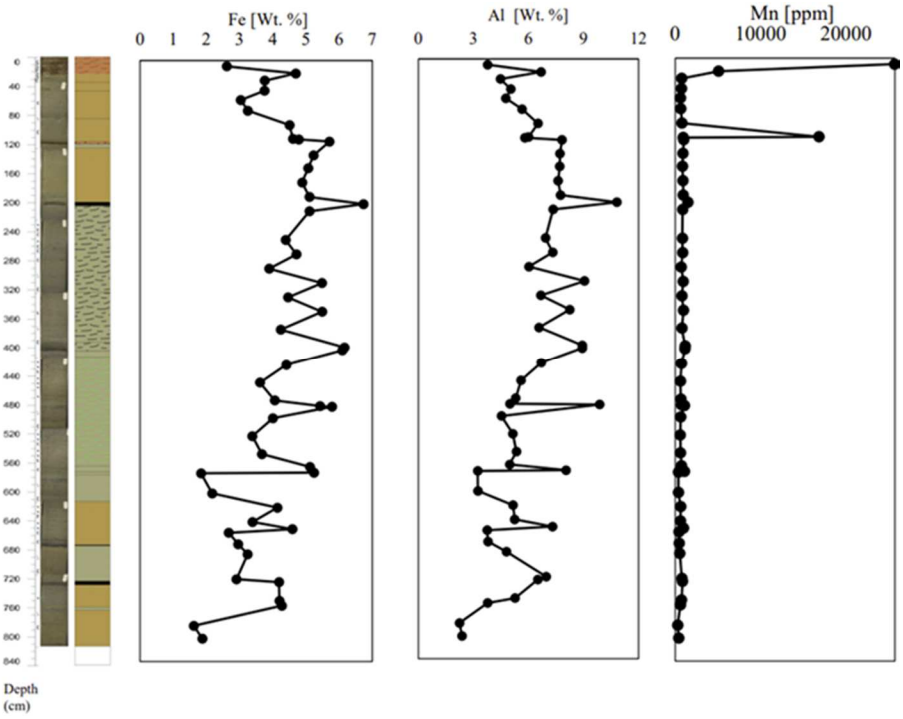

Figure 3: Core photographs, lithology, and elemental concentration data of iron (Fe), aluminum (Al), and manganese (Mn) for Core 18-2. Dark layers shown in lithology are ash layers. Core photos and lithology from Bohrmann (2019).

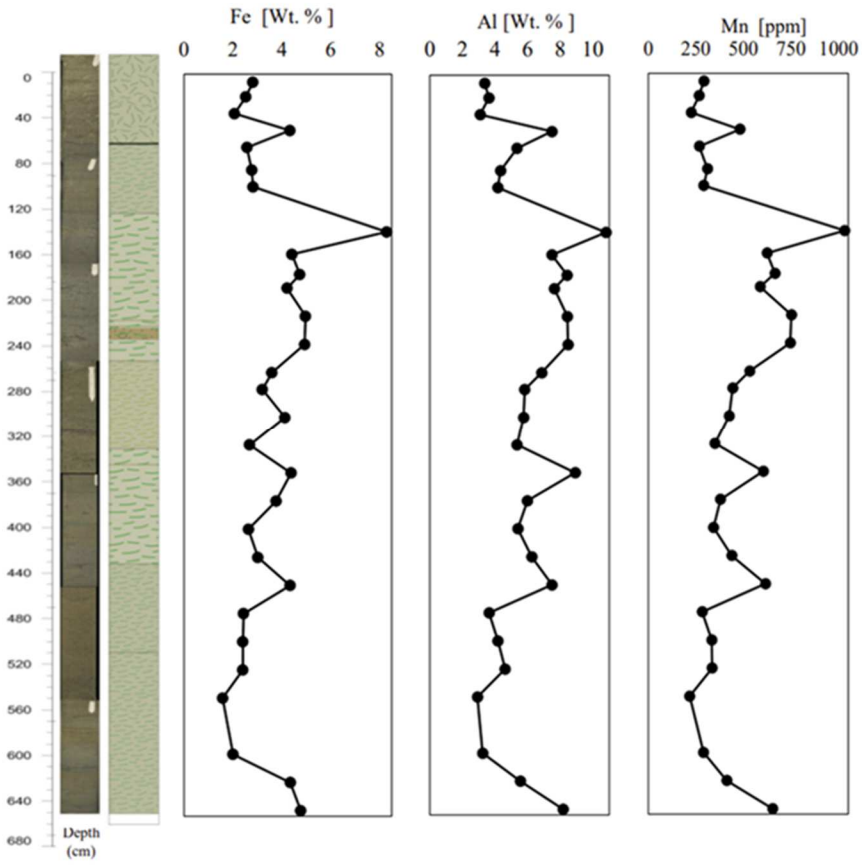

Figure 4: Core photos, lithology, and elemental concentration of iron (Fe), aluminum (Al), and manganese (Mn) for Core 22-1. Dark layers shown in lithology are ash layers. Core photos and lithology from Bohrmann (2019).

Trace Metal Composition

The molybdenum graph of Core 18-2 has two main peaks, at 8 cm and 109 cm (Figure 5). Peaks are not found in the Core 22-1 graph for molybdenum (Figure 6). The molybdenum concentration in Core 22-1 is smaller overall than the concentration of molybdenum in Core 18-2. The maximum concentration of molybdenum in Core 18-2 is 19 ppm at 8 cm while the maximum

concentration in Core 22-1 is only 0.57 ppm at 330 cm. Unlike Core 22-1, Core 18-2 appears to have two separate concentration magnitudes after the 109 cm peak: from approximately 190 cm to 568 cm, the concentration is overall less than the concentrations of Mo from approximately 576 cm to 808 cm (Figure 5). The average concentration of molybdenum in Core 22-1 remains constant throughout the whole measured sediment column.

The concentration spike at 109 cm seen in many of the graphs is not seen in the graph for Core 18-2 uranium concentration. The range of uranium concentrations in Core 18-2 is much lower than the range of other trace metals at Core 18-2 (0.61 ppm to 4.2 ppm). The range of uranium concentrations in Core 22-1 is ranging from 1.6 ppm to 5.4 ppm, which is also a low range compared to the range of other trace metal concentrations in Core 22-1. Both Core 18-2 and Core 22-1 uranium concentrations remain small compared to other trace metal concentrations and constant (Figure 5 and Figure 6).

The copper graph of Core 18-2 has one significant peak at 109 cm, which is at the same depth as one of the peaks in the core 18 molybdenum graph (Figure 5). This peak is not present in Core 22-1. Like molybdenum, the concentration of copper in Core 22-1 is smaller than the concentration of copper in Core 18-2. In the Core 22-1 copper graph, the maximum concentration is 114 ppm at 330 cm, which is much smaller than the maximum concentration of copper in Core 18-2, which is 788 ppm (Figure 5 and Figure 6). The average concentration of copper after the peak in Core 18-2 is similar in magnitude (81 ppm) to the average concentration of copper in Core 22-1 (56 ppm).

The Core 18-2 cobalt concentration graph has the same peak at 109 cm as copper and molybdenum (Figure 5). In the Core 22-1 cobalt concentration graph, the largest peak is at 140

cm, which is shallower than the peak of copper concentrations in Core 22-1 (Figure 6). Both the Core 18-2 and Core 22-1 cobalt concentration graphs remain at a similar constant concentration for the remainder of the measured sediment column.

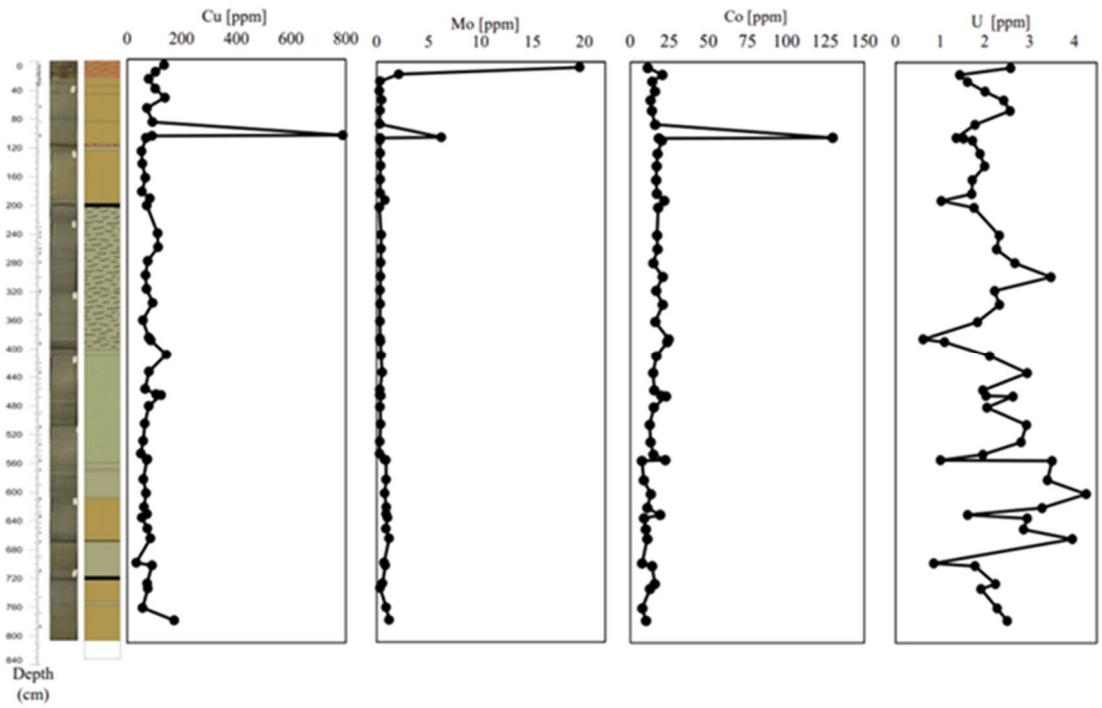

Figure 5: Elemental concentration of copper (Cu), molybdenum (Mo), copper (Co), and uranium (U) for Core 18-2. Core photos and lithology from Bohrmann (2019).

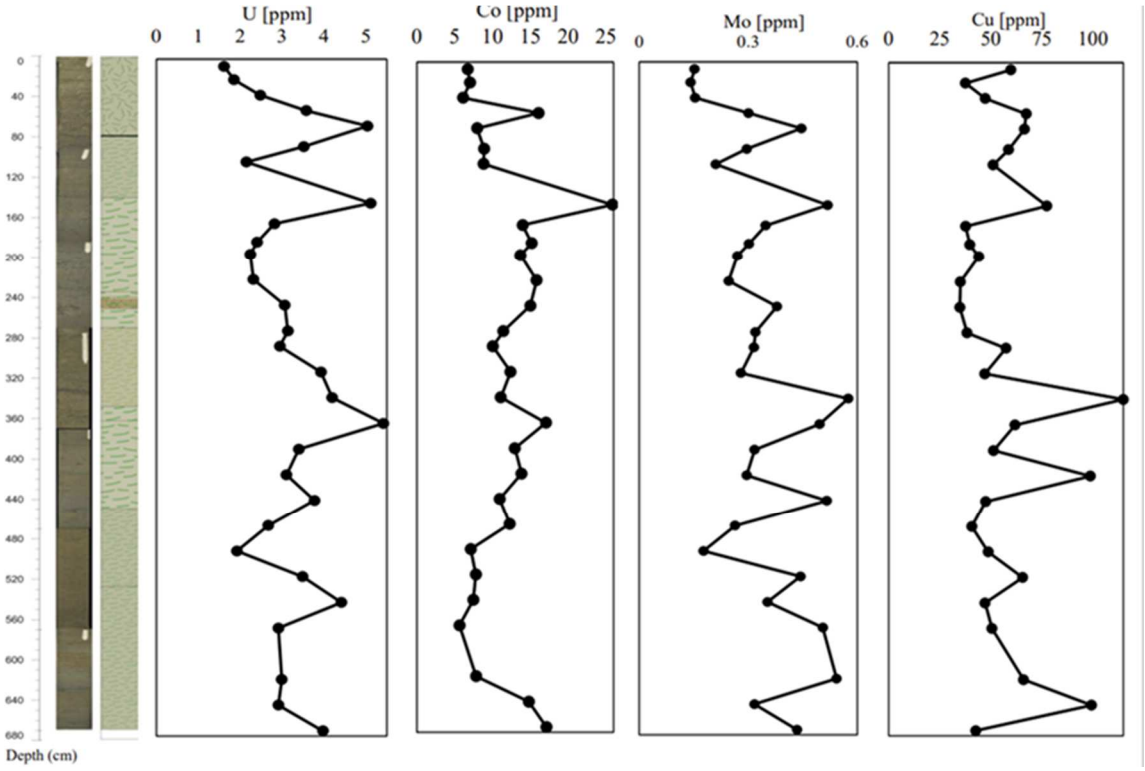

Figure 6: Elemental concentration of uranium (U), cobalt (Co), molybdenum (Mo), and copper (Cu) for Core 22-1. Core photos and lithology from Bohrmann (2019).

Iron Extraction

Iron concentrations from sequential iron extraction on Core 18-2 and Core 22-1 yield 3 different graphs to examine in relation to iron concentration: extraction by ascorbate (Fe-Asc), dithionite (Fe-Dith), and hydrochloric acid (Fe-HCl). The graph for Core 18-2 iron from ascorbate has concentration peaks at 8 cm, 109 cm, and 755 cm (Figure 7). The graph for iron from ascorbate from Core 22-1 has two peaks at 140 cm and 305 cm (Figure 8). The average concentration of iron from ascorbate from Core 22-1 and Core 18-2 are both within 100 ppm of each other (the

Core 18-2 average is 535 ppm, and the Core 22-1 average is 472 ppm). The graph for iron from dithionite in Core 18-2 does not have any clear one sample peaks, however, does increase in concentration from 110 cm to 190 cm (Figure 7). On the contrary, the dithionite graph for Core 22-1 possesses one clear peak at 7 cm (Figure 8). Both iron concentrations from dithionite from Core 22-1 and Core 18-2 are similar in concentration and are both higher in concentration than the iron measured from ascorbate from both cores. The graph for iron concentration measured from hydrochloric acid for Core 18-2 has one clear peak at 755 cm (Figure 7). The graph for iron concentration measured from hydrochloric acid for Core 22-1 has one peak at 178 cm (Figure 8). The average iron concentration measured from hydrochloric acid for Core 22-1 is approximately 500 ppm more than the average iron concentration for Core 18-2.

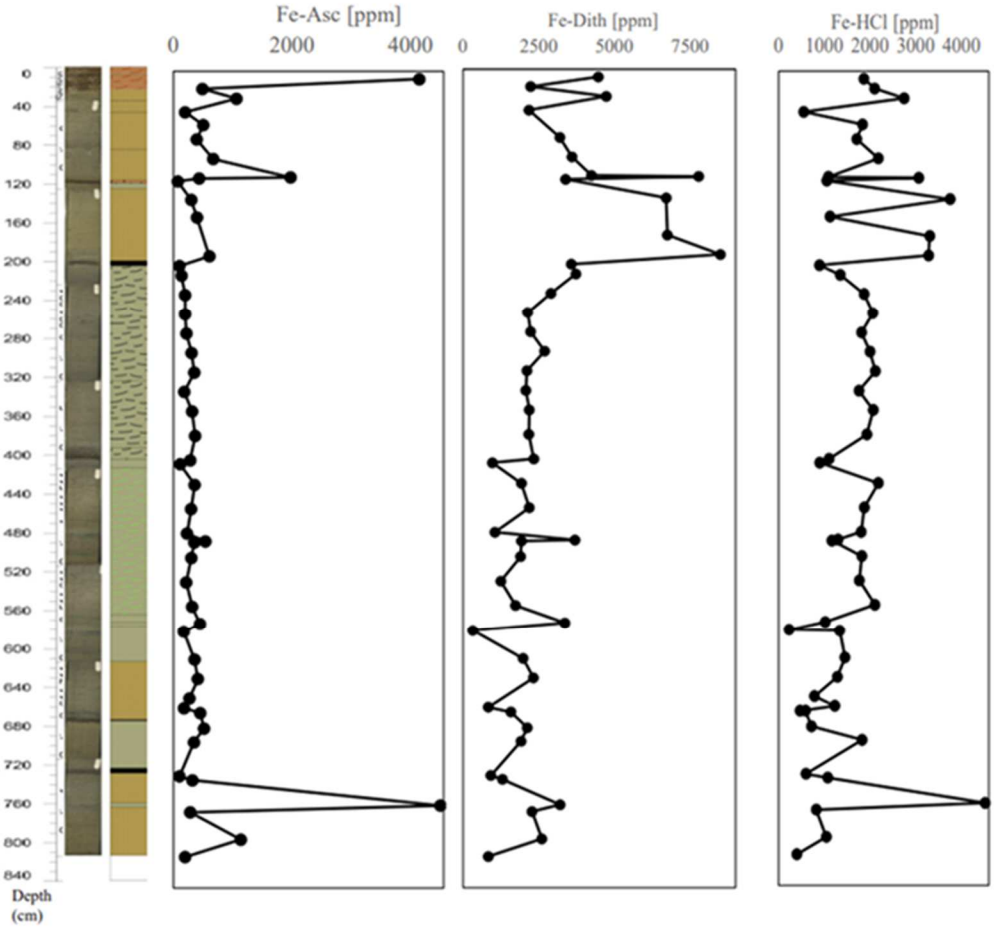

Figure 7: Iron speciation concentration data including the ascorbic phase (Fe-Asc), dithionite phase (Fe-Dith), and iron extracted with hydrochloric acid (Fe-HCl) for Core 18-2. Core photos and lithology from Bohrmann (2019).

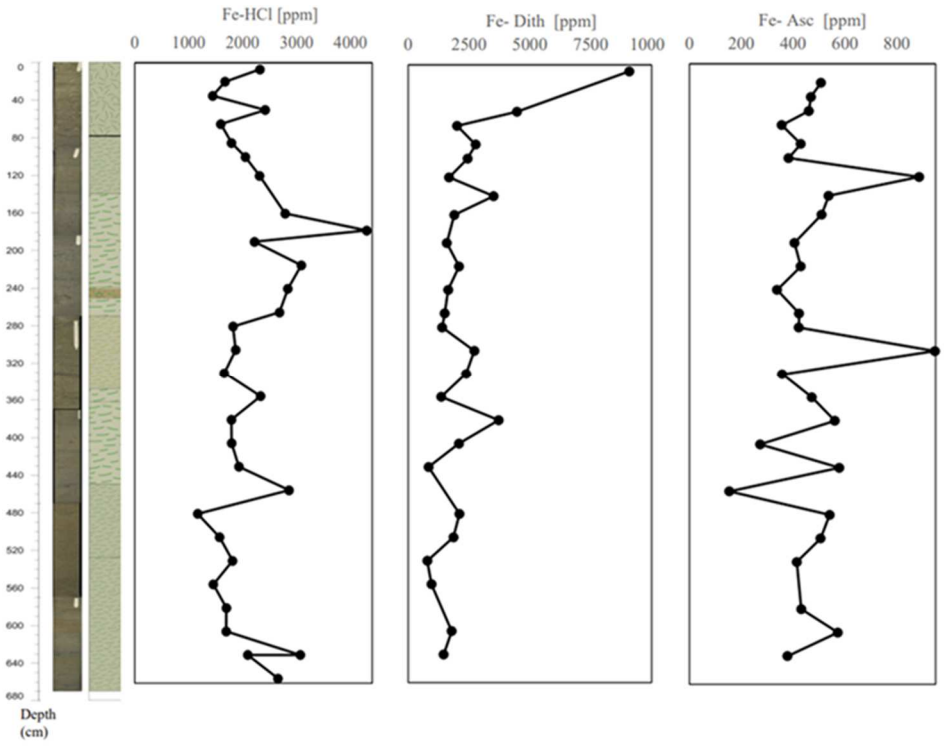

Figure 8: Iron speciation concentration data including the ascorbic phase (Fe-Asc), dithionite phase (Fe-Dith), and iron extracted with hydrochloric acid (Fe-HCl) for Core 22-1. Core photos and lithology from Bohrmann (2019).

The two observable peaks for Core 18-2 are at 8 cm and109 cm (Table 2). The depth with the most peaks among the elements in Core 18-2 is 109 cm with 5 different elements.

Table 2: Comparison of specific metal enrichment layers from Core 18-2 (Fe-total – total iron from ICP-MS analysis, Fe-Asc- iron from the ascorbic phase, Fe-Dith – iron from the dithionite phase, Fe-HCl – iron from hydrochloric acid iron speciation).

Peak (cm)	Mo	U	Cu	Co	Al	Mn	Fe-total	Fe-Asc	Fe-Dith	Fe-HCl
8	X					X		X		
109	X		X	X		X		X		

The two observable peaks with multiple elements for Core 22-1 are found at 140 cm and 330 cm (Table 3). The depth with the most peaks among the elements in Core 22-1 is 140 cm with 3 different elements and 6 different measurable parameters. It is important to observe which element concentrations peak at the same depth because these peaks correspond to different enrichment sources and events, especially because specific elements covary with each other. The discussion section will examine possible sources of these peaks, given which elements covary with each other.

Table 3: Comparison of specific metal enrichment layers from Core 22-1 (Fe-total – total iron from ICP-MS analysis, Fe-Asc- iron from the ascorbic phase, Fe-Dith – iron from the dithionite phase, Fe-HCl – iron from hydrochloric acid iron speciation).

Peak (cm)	Mo	U	Cu	Co	Al	Mn	Fe-Total	Fe-Asc	Fe-Dith	Fe-HCl
140		X		X	X	X	X	X		
330	X	X	X			X		X		

CHAPTER V

DISCUSSION

When comparing the elemental concentrations of Core 18-2 and Core 22-1, there are key differences between magnitude of concentration and peaks in concentration. Peaks are specific enrichment of multiple elements in the same depth sample. These peaks indicate a specific source that was present at the time of deposition but is not present throughout the core. Differences between the cores indicate different sources of metals and elements between the sites.

The average elemental concentrations of Core 22-1 without the elemental peaks (at 140 cm and 330 cm) can be treated as the background concentration of the Scotia Sea and these background concentrations can be compared to Core 18-2 concentrations (Figure 9). Core 22-1 concentrations can be treated as background concentrations because the level of productivity is similar to Core 18-2. It is not likely that productivity activity would vary much between the two sites because they are only approximately 90 km away from each other. The average aluminum concentration of Core 18-2 is only about 4% higher than the average aluminum concentration of Core 22-1, which is indicative of similar detrital input. Average Core 18-2 elemental concentrations are generally higher than average elemental concentrations of Core 22-1. The average molybdenum concentration in Core 18-2 is approximately 69% higher than the background molybdenum concentration calculated from Core 22-1 and the concentrations of molybdenum in Core 18-2 is often above the background concentration, especially deeper in the core (Figure 9).

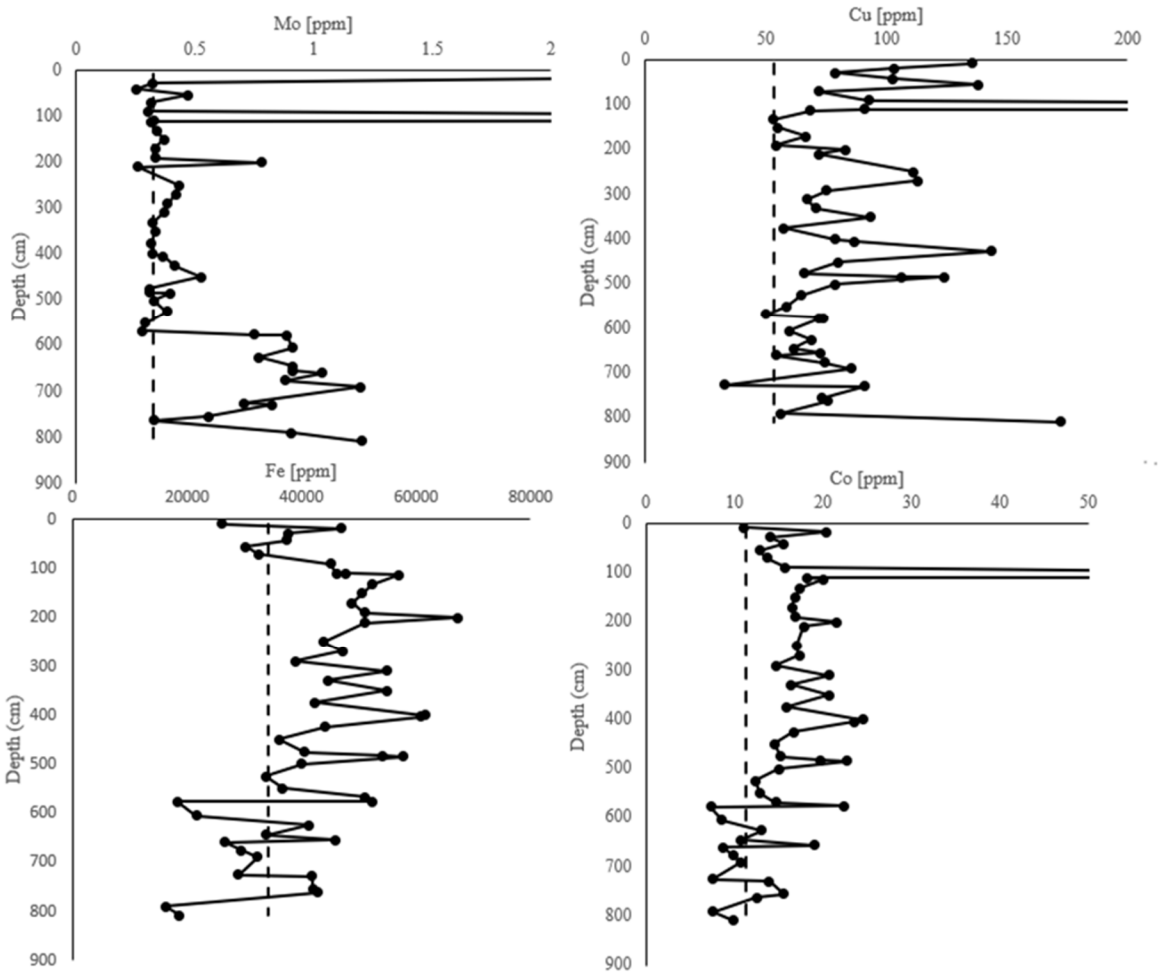

Figure 9: Core 18-2 iron (Fe), cobalt (Co), copper (Cu), and molybdenum (Mo) concentrations with background concentration in dotted line. The background concentration is the average elemental concentrations of Core 22-1 excluding data from the two peaks, 140 cm and 330 cm.

The average copper concentration in Core 18-2 is approximately 44% higher than the background copper and most copper concentrations in Core 18-2 are above the background concentration which suggests extra sources of copper to the sediments at Site 18 (Figure 9). Additionally, the average iron concentration of Core 18-2 is approximately 20% higher than the background iron and much of the iron concentrations are above the background concentrations (Figure 9). The

source supplying extra copper to Core 18-2 may be the same source providing extra iron. The average cobalt concentration in Core 18-2 is approximately 36% higher than the background cobalt and most of the cobalt concentrations in Core 18-2 are above background concentration (Figure 9). The higher average elemental concentrations in Core 18-2 mean that there is an additional constant source of these elements at Site 18 that is not present at Site 22.

The enrichment of metals in Core 18-2 are likely the result of migration of hydrothermal vent fluid to the site from the E2 vent field. Large amounts of iron and other trace metals can be found in hydrothermal fluid as it is gained from the host rock inside the vent (Hawkes et al. 2013). Additionally, hydrothermal vent fluid plumes are often rich in Mn and Fe (oxyhydr)oxides that can adsorb to trace metals (Sanders and Koschinsky 2011, Swanner et al. 2011). The metals that adsorb to the (oxyhydr)oxides can come from the surrounding water or the hydrothermal vent fluids that rise into a buoyant plume (Swanner et al. 2011).

The average uranium concentration from Core 18-2 is the only paleo-proxy that is lower than the background concentration by approximately 41% (Figure 10). The lack of uranium enrichment in Core 18-2 makes sense because uranium does not adsorb to Mn and Fe (oxyhydr)oxides, therefore would not be carried in large concentrations by hydrothermal vent plumes (Algeo and Maynard 2004).

The top of the sediment column for Core 18 and Core 22 are affected by diagenetic alteration that can increase the concentration of elements in the suboxic zone of sediment. In Core 18-2, there is a peak of molybdenum and manganese at 8 cm (Figure 3 and Figure 5). In Core 22-1, there are increases in manganese, iron, cobalt, and copper at 50 cm (Figure 4 and Figure 6). These peaks are most likely the result of diagenetic alteration of Mn and Fe oxides at the surface of the sediment. Manganese cycling can lead to large concentrations of manganese, iron, and metals being deposited near the surface of the ocean floor (Froelich et al. 1979). In the deeper sediment

layers, these oxides are microbially reduced, releasing Mn and Fe as well as adsorbed metals into the pore water (Froelich et al. 1979).

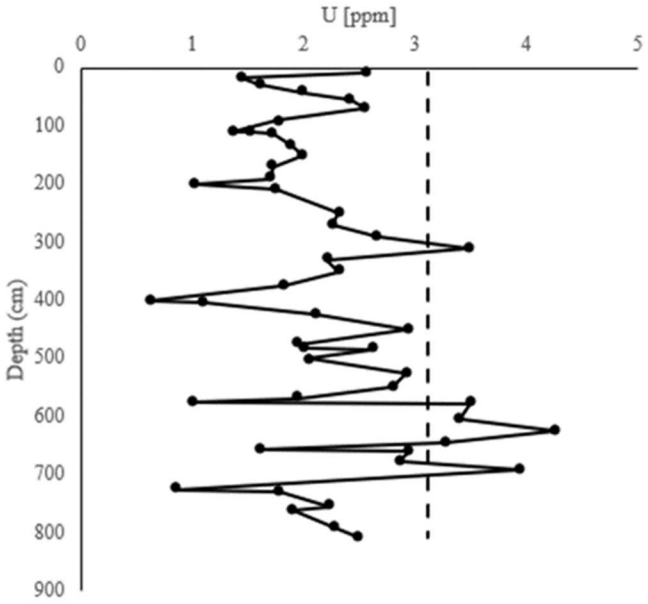

Figure 10: Core 18-2 uranium (U) concentration with background concentration (the average elemental concentrations of Core 22-1) in dotted line.

One potential source of concentration peaks in both Core 18-2 and Core 22-2 is volcanic ash deposits. The concentration peaks of molybdenum, copper, cobalt, manganese, and iron at 109 cm in Core 18-2 could be the result of volcanic ash deposits (Table 2). To the east of the hydrothermal vent field at Site 18 are the South Sandwich Islands, which is a volcanic arc system (Bohrmann 2019). Active volcanism in all volcanoes except for one in the arc has been reported since 1990 (Liu et al. 2021). One volcano on Saunders Island, St. Michael, is reported to be continuously expelling volcanic gas since at least 1820 (Liu et al. 2021). The ash deposits from the volcanic activity in the arc could have been deposited near Core 18-2, depending on how far the ash traveled in the atmosphere before dropping into the water. The concentration peak of iron, copper, aluminum, and uranium at 140 cm in Core 22-1and the concentration peaks of

molybdenum, uranium, copper, iron, and manganese at 330 cm in Core 22-1 may be due to volcanic ash deposits (Table 3). Volcanic ash can increase marine primary productivity because it contains nutrients such as iron, silica, phosphorus, and nitrogen (Lin et al. 2011, Olgun et al. 2013). In a past study of volcanic gasses and lava, iron, copper, cobalt, manganese, and molybdenum were found (Zelenski et al. 2014). In the lava of the Plosky Tolbachik volcano, the concentration of iron was 84,000 ppm, the concentration of copper was 280 ppm, the concentration of cobalt was 26 ppm, and the concentration of molybdenum was 1.9 ppm (Zelenski et al. 2014). While the concentrations of these elements in the volcanic ash are likely lower than the concentrations found in the lava, they are likely present. It is possible that the volcanic ash of nearby volcanoes is responsible for redox and productivity proxy enrichment in both Core 18-2 and Core 22-1. To the southwest of both sites is the Bransfield Strait, which is the site of many active volcanoes (Moreton and Smillie 2017). Past analysis discussed the occurrence of tephra layers from the strait, particularly Deception Island, in the South Scotia Sea (Moreton and Smillie 2017). This is important because it illustrates that volcanic ash has the range to be deposited to either site.

Summary and Conclusion

Overall, Core 18-2, east of the hydrothermal vent, has higher concentrations of the redox and productivity proxies than Core-22-1, apart from uranium. Sediments at Site 22 are dominated by siliceous ooze with likely minor input of volcanic ash deposits. However, our results suggest no or negligible input from hydrothermal vent fluids on the western side of the ESR. The higher average concentration of metals in Core 18-2 indicates a constant source of enrichment that Core 22-1 is not receiving. Thus, concentrations of iron, molybdenum, copper, and cobalt at Site 18 are likely enriched due to hydrothermal vent plumes from the E2 vent field. The hydrothermal vent

fluids form buoyant plumes and mix with water and diffuse flow (German and Seyfried 2014). Metals from the vent fluid and seawater are adsorbed to Mn and Fe (oxydr)oxides created in the plume and transported to the sediment surface due to precipitation (Mandernack and Tebo 1993, Hawkes et al. 2013). Metals from the vent fluids can be transported via the plume away from the vent site via currents and deposited to the ocean floor (Sander and Koshinksky 2011, German et al. 2015, Pereira et al. 2022). Uranium is not enriched by hydrothermal vent fluids because it does not adsorb oxyhydr)oxides and is not enriched in hydrothermal vent fluids (Algeo and Maynard 2004, German and Seyfried 2014). Other sources attributed to elevated concentrations in both cores are volcanic ash deposits which originate from the nearby volcanic island arc. Additionally, early diagenetic alteration can lead to enrichment layers in the uppermost sediments.

The presence of hydrothermal vent fluid input in Core 18-2 has implications for paleoenvironmental proxy applications in ancient sediment. An enrichment of these metals could alter interpretations of the proxies if potential hydrothermal vent sources are not considered before interpreting the proxies for productivity and redox conditions. Therefore, hydrothermal vent inputs are an important source to consider when analyzing concentrations of productivity proxies and redox proxies. Ancient hydrothermal vents could be buried after a long period of inactivity and sediment deposition. If an ancient sediment core displays an enrichment peak of these metals, it may not be immediately apparent if the enrichment is due to water column changes or a hydrothermal source. It is important to consider hydrothermal input as a potential source of metal enrichment in the sediment core and study the site carefully when hydrothermal vents may be active.

REFERENCES

Abshire, M. L., Romaniello, S. J., Kuzminov, A. M., Cofrancesco, J., Severmann, S., & Riedinger, N. (2020). Uranium isotopes as a proxy for primary depositional redox conditions in organic-rich marine systems. *Earth and Planetary Science Letters*, *529*, 115878.

Algeo, T. J., & Liu, J. (2020). A re-assessment of elemental proxies for paleoredox analysis. *Chemical Geology*, *540*, 119549.

Algeo, T. J., & Maynard, J. B. (2004). Trace-element behavior and redox facies in core shales of Upper Pennsylvanian Kansas-type cyclothems. *Chemical geology*, *206*(3-4), 289-318.

Algeo, T. J., & Tribovillard, N. (2009). Environmental analysis of paleoceanographic systems based on molybdenum–uranium covariation. *Chemical Geology*, *268*(3-4), 211-225.

Bennett, W. W., & Canfield, D. E. (2020). Redox-sensitive trace metals as paleoredox proxies: a review and analysis of data from modern sediments. *Earth-Science Reviews*, *204*, 103175.

Berger, W & Smetacek, Victor & Wefer, Gerold. (1989). Ocean productivity and paleoproductivity - An overview. *Productivity in the Ocean - Present and Past*. John Wiley. Pages. 1-34.

Bischoff JL and Rosenbauer RJ (1985) An empirical equation of state for hydrothermal seawater (3.2% NaCl). *American Journal of Science* 285: 725–763

Bohrmann, G. (2019). The Expedition PS119 of the Research Vessel POLARSTERN to the Eastern Scotia Sea in 2019, Berichte zur Polar- und Meeresforschung = Reports on polar and marine research, Bremerhaven, Alfred Wegener Institute for Polar and Marine Research, 736, 236 p. doi: 10.2312/BzPM_0736_2019

Bruland, K. W. & Lohan, M. C. (2006). Controls of trace metals in seawater. *The oceans and marine geochemistry*, *6*, 23-47.

Calvert, S. E., & Pedersen, T. F. (1993). Geochemistry of recent oxic and anoxic marine sediments: implications for the geological record. *Marine geology*, *113*(1-2), 67-88.

Garabato, A. C. N., Heywood, K. J., & Stevens, D. P. (2002). Modification and pathways of Southern Ocean deep waters in the Scotia Sea. *Deep Sea Research Part I: Oceanographic Research Papers*, *49*(4), 681-705.

German, C. R., Livermore, R. A., Baker, E. T., Bruguier, N. I., Connelly, D. P., Cunningham, A. P. & Tyler, P. A. (2000). Hydrothermal plumes above the East Scotia Ridge: an isolated high-latitude back-arc spreading centre. *Earth and Planetary Science Letters*, *184*(1), 241-250.

German, C.R, Seyfried, W.E. (2014) 8.7 - Hydrothermal Processes, Editor(s): Heinrich D. Holland, Karl K. Turekian, *Treatise on Geochemistry (Second Edition)* Elsevier. 2014. Pages 191-233, ISBN 9780080983004, https://doi.org/10.1016/B978-0-08-095975-7.00607-0

German, C. R., Legendre, L. L., Sander, S. G., Niquil, N., Luther Iii, G. W., Bharati, L.,& Le Bris, N. (2015). Hydrothermal Fe cycling and deep ocean organic carbon scavenging: model-based evidence for significant POC supply to seafloor sediments. *Earth and Planetary Science Letters*, *419*, 143-153.

German, C. R., Casciotti, K. A., Dutay, J. C., Heimbürger, L. E., Jenkins, W. J., Measures, C. I., & Whitby, H. (2016). Hydrothermal impacts on trace element and isotope ocean biogeochemistry. *Philosophical Transactions of the Royal Society A: Mathematical, Physical and Engineering Sciences*, *374*(2081), 20160035.

Fernex, F., Février, G., Bénaïm, J., & Arnoux, A. (1992). Copper, lead and zinc trapping in Mediterranean deep-sea sediments: probable coprecipitation with Mn and Fe. *Chemical Geology*, *98*(3-4), 293-306.

Froelich, P., Klinkhammer, G. P., Bender, M. L., Luedtke, N. A., Heath, G. R., Cullen, D. & Maynard, V. (1979). Early oxidation of organic matter in pelagic sediments of the eastern equatorial Atlantic: suboxic diagenesis. *Geochimica et cosmochimica acta*, *43*(7), 1075-1090.

Halbach, P., Friedrich, G., & von Stackelberg, U. (Eds.). (1988). *The manganese nodule belt of the Pacific Ocean: geological environment, nodule formation, and mining aspects* (pp. 51-56). F. Enke.

Hawkes, J. A., Connelly, D. P., Gledhill, M., & Achterberg, E. P. (2013). The stabilisation and transportation of dissolved iron from high temperature hydrothermal vent systems. *Earth and Planetary Science Letters*, *375*, 280-290.

Helfrich KR and Speer KG (1995) Ocean hydrothermal circulation: Mesoscale and basin-scale flow. *Seafloor Hydrothermal Systems: Physical, Chemical, Biological, and Geological Interactions, Geophysical Monograph Series*, vol. 91, pp. 347–356. Washington, DC: American Geophysical Union.

Helz, G.R., Miller, C.V., Charnock, J.M., Mosselmans, J.F.W., Pattrick, R.A.D., Garner, C.D. and Vaughan, D.J., 1996. Mechanism of molybdenum removal from the sea and its concentration in black shales: EXAFS evidence. Geochimica et Cosmochimica Acta, 60(19), pp.3631-3642.

Hrischeva, E., & Scott, S. D. (2007). Geochemistry and morphology of metalliferous sediments and oxyhydroxides from the Endeavour segment, Juan de Fuca Ridge. *Geochimica et Cosmochimica Acta*, *71*(14), 3476-3497.

James, R. H., Green, D. R., Stock, M. J., Alker, B. J., Banerjee, N. R., Cole, C., & Connelly, D. P. (2014). Composition of hydrothermal fluids and mineralogy of associated chimney material on the East Scotia Ridge back-arc spreading centre. *Geochimica et Cosmochimica Acta*, *139*, 47-71.

Leat, P. T., Livermore, R. A., Millar, I. L., & Pearce, J. A. (2000). Magma supply in back-arc spreading centre segment E2, East Scotia Ridge. *Journal of Petrology*, *41*(6), 845-866.

Lin, I. I., Hu, C., Li, Y. H., Ho, T. Y., Fischer, T. P., Wong, G. T., ... & Chen, J. P. (2011). Fertilization potential of volcanic dust in the low□nutrient low□chlorophyll western North Pacific subtropical gyre: Satellite evidence and laboratory study. *Global Biogeochemical Cycles*, *25*(1).

Little, S. H., Vance, D., McManus, J., Severmann, S., & Lyons, T. W. (2017). Copper isotope signatures in modern marine sediments. *Geochimica et Cosmochimica Acta*, *212*, 253-273.

Lyons, T. W., Anbar, A. D., Severmann, S., Scott, C., & Gill, B. C. (2009). Tracking euxinia in the ancient ocean: a multiproxy perspective and Proterozoic case study. *Annual Review of Earth and Planetary Sciences*, *37*(1), 507-534.

Maldonado, A., Dalziel, I.W. and Leat, P.T., 2015. The global relevance of the Scotia Arc: an introduction. *Global and Planetary Change*, 125, pp. A1-A8.

Mandernack, K. W., & Tebo, B. M. (1993). Manganese scavenging and oxidation at hydrothermal vents and in vent plumes. *Geochimica et Cosmochimica Acta*, *57*(16), 3907-3923.

Mantyla, A. W., & Reid, J. L. (1983). Abyssal characteristics of the World Ocean waters. *Deep Sea Research Part A. Oceanographic Research Papers*, *30*(8), 805-833.

McManus, J., Berelson, W. M., Severmann, S., Poulson, R. L., Hammond, D. E., Klinkhammer, G. P., & Holm, C. (2006). Molybdenum and uranium geochemistry in continental margin sediments: paleoproxy potential. *Geochimica et Cosmochimica acta*, *70*(18), 4643-4662.

Morford, J. L., & Emerson, S. (1999). The geochemistry of redox sensitive trace metals in sediments. *Geochimica et Cosmochimica Acta*, *63*(11-12), 1735-1750.

Morse, J. W., & Luther Iii, G. W. (1999). Chemical influences on trace metal-sulfide interactions in anoxic sediments. *Geochimica et Cosmochimica Acta*, *63*(19-20), 3373-3378.

Olgun N., Duggen S., Andronico D., Kutterolf S., Croot P., Giammanco S., Censi P., Randazzo P. (2013) Possible impacts of volcanic ash emissions of Mount Etna on the primary productivity in the oligotrophic Mediterranean Sea: Results from nutrient-release experiments in seawater, *Marine Chemistry*, Volume 152, Pages 32-42

Pereira, S. I., Diehl, A., McDermott, J. M., Pape, T., Klose, L., Strauss, H., & Bach, W. (2022). Geochemistry of hydrothermal fluids from the E2-segment of the East Scotia Ridge: Magmatic input, reaction zone processes, fluid mixing regimes and bioenergetic landscapes. *Frontiers in Marine Science*, *9*, 765648.

Poulton, S. W., & Canfield, D. E. (2005). Development of a sequential extraction procedure for iron: implications for iron partitioning in continentally derived particulates. *Chemical geology*, *214*(3-4), 209-221.

Raiswell, R., Vu, H. P., Brinza, L., & Benning, L. G. (2010). The determination of labile Fe in ferrihydrite by ascorbic acid extraction: methodology, dissolution kinetics and loss of solubility with age and de-watering. *Chemical Geology*, *278*(1-2), 70-79.

Rogers, A. D., Tyler, P. A., Connelly, D. P., Copley, J. T., James, R., Larter, R. D., & Zwirglmaier, K. (2012). The discovery of new deep-sea hydrothermal vent communities in the Southern Ocean and implications for biogeography. *PLoS biology*, *10*(1), e1001234.

Sander, S. G., & Koschinsky, A. (2011). Metal flux from hydrothermal vents increased by organic complexation. *Nature Geoscience*, *4*(3), 145-150.

Saito, M. A., Moffett, J. W., & DiTullio, G. R. (2004). Cobalt and nickel in the Peru upwelling region: A major flux of labile cobalt utilized as a micronutrient. *Global Biogeochemical Cycles*, *18*(4).

SCOR Working Group. (2007). GEOTRACES–An international study of the global marine biogeochemical cycles of trace elements and their isotopes. *Geochemistry*, *67*(2), 85-131.

Scott, C. and Lyons, T.W., 2012. Contrasting molybdenum cycling and isotopic properties in euxinic versus non-euxinic sediments and sedimentary rocks: Refining the paleoproxies. *Chemical Geology*, 324, pp.19-27.

Severmann, S., Johnson, C. M., Beard, B. L., & McManus, J. (2006). The effect of early diagenesis on the Fe isotope compositions of porewaters and authigenic minerals in continental margin sediments. *Geochimica et Cosmochimica Acta*, *70*(8).

Steiner, Z., Lazar, B., Torfstein, A., & Erez, J. (2017). Testing the utility of geochemical proxies for paleoproductivity in oxic sedimentary marine settings of the Gulf of Aqaba, Red Sea. *Chemical Geology*, *473*, 40-49.

Stookey, L. L. (1970). Ferrozine---a new spectrophotometric reagent for iron. *Analytical chemistry*, *42*(7), 779-781.

Swanner, E. D., Planavsky, N. J., Lalonde, S. V., Robbins, L. J., Bekker, A., Rouxel, O. J., & Konhauser, K. O. (2014). Cobalt and marine redox evolution. *Earth and Planetary Science Letters*, *390*, 253-263.

Tribovillard, N., Algeo, T. J., Lyons, T., & Riboulleau, A. (2006). Trace metals as paleoredox and paleoproductivity proxies: an update. *Chemical geology*, *232*(1-2), 12-32.

Yeo, I. (2014). Axial Volcanic Ridges. *Encyclopedia of Marine Geosciences*. Springer Science. DOI: 10.1007/978-94-007-6644-0_2-2.

Yücel, M., Gartman, A., Chan, C. S., & Luther, G. W. (2011). Hydrothermal vents as a kinetically stable source of iron-sulphide-bearing nanoparticles to the ocean. *Nature Geoscience*, *4*(6), 367-371.

APPENDICES

Table A1: Solid phase data for Core 18-2.

Sample #	Depth (cm)	Al [wt. %]	Mn [ppm]	Fe [wt. %]	Co [ppm]	Cu [ppm]	Mo [ppm]	U [ppm]
123	8	3.77	25680.5	2.61	11.1	135.7	19.55	2.57
124	18	6.69	5082.4	4.70	20.4	103.6	2.13	1.44
125	28	4.47	763.8	3.76	14.0	79.1	0.32	1.61
126	42	5.04	723.5	3.75	15.6	102.8	0.25	2.00
127	55	4.77	621.8	3.03	12.9	138.0	0.47	2.42
128	70	5.65	648.4	3.25	13.7	72.4	0.32	2.56
129	90	6.52	796.6	4.51	15.8	92.8	0.30	1.78
159	109	6.01	16834.3	4.61	129.6	788.7	6.21	1.36
130	110	5.80	928.9	4.78	18.2	91.1	0.33	1.52
160	113	7.83	989.9	5.71	20.1	68.6	0.32	1.72
131	132	7.72	904.3	5.23	17.4	53.0	0.34	1.89
132	150	7.71	842.9	5.07	16.8	55.3	0.37	1.99
133	170	7.62	911.1	4.89	16.5	66.7	0.33	1.72
134	190	7.75	936.0	5.11	17.0	54.4	0.33	1.71
161	200	10.82	1474.9	6.74	21.6	82.9	0.78	1.02
135	210	7.34	871.6	5.11	17.8	72.1	0.26	1.75
137	250	6.93	829.7	4.39	17.0	111.5	0.43	2.32
138	270	7.32	871.7	4.72	17.4	113.0	0.42	2.26
139	290	6.03	700.9	3.89	14.7	75.2	0.39	2.67
140	310	9.06	938.4	5.48	20.7	67.1	0.37	3.48
141	330	6.68	774.5	4.46	16.5	71.2	0.32	2.22

Table A1 Continued

Sample #	Depth (cm)	Al [wt. %]	Mn [ppm]	Fe [wt. %]	Co [ppm]	Cu [ppm]	Mo [ppm]	U [ppm]
142	350	8.25	962.5	5.49	20.7	93.5	0.33	2.32
143	375	6.58	778.6	4.24	15.9	57.6	0.32	1.83
144	400	8.93	1154.1	6.16	24.5	79.0	0.32	0.62
162	404	8.93	1144.7	6.09	23.6	86.6	0.37	1.10
145	425	6.70	732.4	4.41	16.7	143.4	0.42	2.10
146	450	5.60	603.6	3.61	14.5	80.1	0.53	2.94
147	475	5.31	659.2	4.06	15.3	65.8	0.31	1.95
163	483	4.99	731.3	5.42	19.7	106.1	0.31	2.02
172	484	9.88	1076.0	5.78	22.8	123.9	0.40	2.62
148	500	4.53	630.7	4.00	15.0	79.0	0.33	2.04
149	525	5.15	583.4	3.38	12.3	64.8	0.38	2.93
150	550	5.35	613.2	3.67	12.9	58.8	0.29	2.81
164	568	4.98	736.4	5.12	14.7	50.3	0.28	1.95
165	576	8.05	1065.0	5.25	22.3	73.8	0.75	1.00
151	577	3.24	370.3	1.84	7.4	72.1	0.89	3.50
152	605	3.25	371.8	2.17	8.6	59.6	0.91	3.40
153	625	5.16	638.1	4.14	13.1	69.0	0.77	4.26
166	645	5.25	622.7	3.39	10.8	61.5	0.91	3.27
154	655	7.31	974.0	4.59	19.1	72.8	0.91	1.61
167	660	3.75	447.4	2.67	8.8	54.2	1.04	2.94
168	676	3.79	463.3	2.96	9.8	74.3	0.88	2.86

Table A1 Continued

Sample #	Depth (cm)	Al [wt. %]	Mn [ppm]	Fe [wt. %]	Co [ppm]	Cu [ppm]	Mo [ppm]	U [ppm]
155	690	4.80	535.9	3.24	10.8	85.5	1.20	3.95
156	725	6.96	778.3	2.91	7.5	33.3	0.71	0.85
169	729	6.51	848.9	4.19	13.9	90.9	0.83	1.78
157	755	5.27	733.5	4.20	15.6	73.1	0.56	2.24
170	762	3.77	604.8	4.27	12.6	75.7	0.33	1.91
158	790	2.24	283.6	1.62	7.6	56.5	0.91	2.27
171	808	2.38	415.8	1.88	9.9	172.2	1.20	2.50

Table A2 Iron Extraction Data for Core 18-2.

Sample #	Depth (cm)	Fe-HCl [ppm]	Fe-Ascorbate [ppm]	Fe-Dithionite [ppm]
123	8	1868.3	4152.4	4469.1
124	18	2102.2	485.7	2231.8
125	28	2749.0	1064.1	4735.1
126	42	551.4	195.4	2176.7
127	55	1837.4	499.0	N/A
128	70	1710.4	391.5	3195.4
129	90	2182.4	669.4	3597.1
159	109	1090.8	1977.8	4242.1
130	110	3065.6	433.7	7784.7
160	113	1058.7	69.1	3385.4
131	132	3753.8	299.7	6709.8
132	150	1128.1	394.4	2974.3
133	170	3305.7	NA	6750.4

Table A2 Continued

Sample #	Depth (cm)	Fe-HCl [ppm]	Fe-Ascorbate [ppm]	Fe-Dithionite [ppm]
134	190	3282.1	604.7	8503.2
161	200	895.0	98.0	3575.6
135	210	1349.8	135.2	3729.7
137	250	2063.7	195.5	2903.8
138	270	1814.7	194.9	2134.8
139	290	2001.0	216.4	2233.3
140	310	2118.7	305.3	2694.3
141	330	1760.9	347.9	2108.6
142	350	2069.4	183.0	2072.2
143	375	1931.5	311.6	2185.5
144	400	1107.2	364.2	2173.7

N/A – not analyzed

Table A3 Solid phase data for Core 22-1.

Sample #	Depth (cm)	Al [wt. %]	Mn [ppm]	Fe [wt. %]	Co [ppm]	Cu [ppm]	Mo [ppm]	U [ppm]
202	7	3.37	291.8	2.81	6.7	59.9	0.15	1.61
203	20	3.62	266.8	2.53	7.0	37.6	0.14	1.85
204	35	3.09	225.4	2.06	6.1	47.4	0.15	2.48
205	50	7.48	481.1	4.33	16.1	67.4	0.30	3.58
206	65	5.35	267.6	2.57	8.0	66.5	0.45	5.04
207	85	4.33	310.5	2.77	8.9	58.8	0.30	3.52
208	100	4.17	291.1	2.82	8.8	51.2	0.21	2.15

Table A3 Continued

Sample #	Depth (cm)	Al [wt. %]	Mn [ppm]	Fe [wt. %]	Co [ppm]	Cu [ppm]	Mo [ppm]	U [ppm]
210	140	10.80	1031.5	8.29	25.9	77.5	0.52	5.11
211	160	7.48	623.7	4.41	14.0	37.7	0.35	2.82
212	178	8.42	665.4	4.73	15.2	39.8	0.30	2.40
213	190	7.64	587.6	4.22	13.7	44.1	0.27	2.24
214	215	8.44	751.5	4.97	15.8	35.2	0.25	2.31
215	240	8.47	745.6	4.94	15.0	34.9	0.38	3.06
216	265	6.86	532.6	3.60	11.4	38.5	0.32	3.14
217	280	5.82	443.1	3.20	10.1	57.5	0.32	2.95
218	305	5.75	424.5	4.13	12.4	47.1	0.28	3.93
219	330	5.35	349.8	2.68	11.1	115.0	0.58	4.19
220	355	8.91	603.8	4.38	17.1	61.9	0.50	5.42
221	380	5.99	379.0	3.76	13.0	51.4	0.32	3.40
222	405	5.40	342.6	2.63	13.8	98.8	0.30	3.10
223	430	6.25	438.5	3.02	11.0	47.6	0.52	3.77
224	455	7.49	615.2	4.34	12.3	40.8	0.26	2.67
225	480	3.63	282.7	2.43	7.1	48.8	0.18	1.92
226	505	4.18	333.3	2.40	7.8	65.7	0.44	3.49
227	530	4.62	335.0	2.40	7.5	47.3	0.35	4.42
228	555	2.92	217.1	1.58	5.6	50.6	0.51	2.91
230	605	3.23	289.6	2.00	7.9	66.1	0.54	2.99
231	630	5.55	412.0	4.35	14.8	99.4	0.32	2.91
232	655	8.18	652.8	4.78	17.1	42.7	0.43	3.97

N/A – not analyzed

Table A4 Iron Extraction Data for Core 22-1

Sample #	Depth (cm)	Fe-HCl [ppm]	Fe- Ascorbate [ppm]	Fe- Dithionite [ppm]
202	7	2319.9	N/A	9081.1
203	20	1673.5	507.3	N/A
204	35	1445.0	468.5	N/A
205	50	2419.6	460.7	4469.5
206	65	1595.5	356.1	2012.9
207	85	1793.1	429.4	2768.3
208	100	2050.5	382.4	2439.9
210	140	2787.8	886.4	1680.9
211	160	4299.4	537.1	3509.5
212	178	2218.0	510.1	1892.9
213	190	3086.8	405.3	1587.1
214	215	2837.3	429.6	2091.3
215	240	2683.2	338.3	1643.7
216	265	1821.5	422.9	1501.8
217	280	1870.8	422.2	1396.7
218	305	1658.4	947.4	2716.2
219	330	2333.7	358.0	2381.9
220	355	1791.9	472.4	1356.8
221	380	1795.3	561.1	3715.3
222	405	1931.0	272.9	2085.6

Table A4 Continued

Sample #	Depth (cm)	Fe-HCl [ppm]	Fe- Ascorbate [ppm]	Fe- Dithionite [ppm]
223	430	2860.9	578.5	836.5
224	455	1167.8	154.1	N/A
225	480	1572.9	541.0	2107.7
226	505	1813.3	505.8	1861.3
227	530	1456.6	414.3	787.6
228	555	1699.4	NA	959.8
230	605	1695.7	431.7	N/A
231	630	3067.4	572.6	1786.4
232	655	2653.9	378.6	1458.4

N/A – not analyzed

Table A5: Replicates and National Institute of Standards and Technology 2702 Inorganics in Seawater Standard Reference Material (NIST2702)

Sample #	Al [ppm]	Mn [ppm]	Fe [ppm]	Co [ppm]	Cu [ppm]	Mo [ppm]	U [ppm]
Sample Replicate 1 (SR1)	5.49	395.5	2.94	9.6	67.5	1.58	6.84
Sample Replicate 2 (SR2)	4.15	299.7	2.29	7.4	51.7	1.22	5.19
Sample Replicate 3 (SR3)	3.70	270.5	2.06	6.5	47.0	1.12	4.67
2702 NIST R1	7.42	1531.8	6.71	22.9	99.5	8.59	9.61
2702 NIST R2	9.49	1971.3	8.68	29.5	128.6	11.12	12.83
NIST 2702 R3	8.58	1815.8	7.95	27.1	118.3	10.07	11.42
NIST2702 certified	*8.41*	*1757.0*	*7.91*	*27.8*	*117.7*	*10.80*	*10.40*

VITA

Alison Veresh

Candidate for the Degree of

Master of Science

Thesis: HYDROTHERMAL VENTS AND THEIR IMPACT ON PALEOENVIRONMENTAL PROXIES

Major Field: Geology

Biographical:

Education:

Completed the requirements for the Master of Science in geology at Oklahoma State University, Stillwater, Oklahoma in December 2022.

Completed the requirements for the Bachelor of Science in environmental science at Central Michigan University, Mount Pleasant, Michigan in 2020.